Spatially resolved macroscopic near-threshold harmonics generated from harmoniclike and resonant transitions using an artificial neural network

Bincheng Wang,[1] Tianyu Wen,[1] Yong Fu,[1] Baochang Li,[1] Kan Wang,[1] and Cheng Jin[1,2,*]

[1]*Experimental Teaching Center of Physics and Department of Applied Physics, Nanjing University of Science and Technology, Nanjing, Jiangsu 210094, China*

[2]*MIIT Key Laboratory of Semiconductor Microstructure and Quantum Sensing, Nanjing University of Science and Technology, Nanjing, Jiangsu 210094, China*

(Received 10 June 2023; accepted 1 November 2023; published 17 November 2023)

We investigate the generation of near-threshold harmonics (NTHs) based on solving the three-dimensional time-dependent Schrödinger equation and utilizing an artificial neural network as a surrogate model to study the macroscopic propagation. Through our research, we identify two distinct pathways for NTH generation: harmoniclike transition and resonant transition. These pathways exhibit varying laser-parameter dependencies and phase-matching conditions, making it possible to spatially separate and selectively enhance NTHs by manipulating laser parameters in experimental setups. Our study provides insights into the underlying physics of the NTH macroscopic propagation and presents a methodology that can be applied to computationally intensive problems in the field of strong-field physics.

DOI: 10.1103/PhysRevA.108.053510

I. INTRODUCTION

High-order harmonic generation (HHG) is a phenomenon that occurs when ultrashort femtosecond intense laser pulses interact with atoms and molecules. It has emerged as a vital aspect of ultrafast science and technology, facilitating significant advancements in the field [1–3]. HHG yields coherent light sources in the extreme-ultraviolet (XUV) to soft-x-ray range that have proven invaluable for various applications [4,5]. Moreover, HHG serves as a valuable tool for investigating atomic and molecular electronic structures and ultrafast dynamics [6–8]. Recently, experiments have shown that near-threshold harmonics (NTHs), which are harmonics generated near the ionization threshold I_p of the target atom, can serve as light sources for VUV frequency-comb applications [9–16]. These breakthroughs have highlighted the potential of NTHs in expanding the range of applications in the VUV spectral region.

Considering that the energy range of NTHs closely overlaps with that of Rydberg states, it is reasonable to question whether the numerous excited states near the ionization threshold have any influence on NTH generation. In a study conducted in 2009, Yost *et al.* explored the generation of the 7th (H7) to 13th (H13) harmonics, which are in close proximity to the ionization threshold, using a 136-MHz, 1070-nm laser on a xenon (Xe) target [10]. The research findings revealed intense intensity-dependent oscillations in the on-axis yields of H7 and H11, while such oscillations were comparatively weaker for H9 and H13. Moreover, the far-field spatial profiles of H7 and H11 exhibited more diffused characteristics (halos), whereas those of H9 and H13 were more focused. This initial investigation provided evidence for the coherence of NTHs and their potential use in applications involving VUV frequency-comb structures. Subsequently, in 2014 NTHs were further examined using a 5-fs, 800-nm driving laser on an argon (Ar) target [12]. In this study the short pulse duration led to the spreading of H9 across the ionization threshold, revealing multiple sharp lines below the threshold. These atomic lines predominated at low intensity, and their positions shifted towards higher energies as the intensity increased. These lines were understood to arise from the coherent radiation decay of Rydberg states trapped in the laser field [17]. However, it was also proposed that they may originate from ionization of excited states recombining to the ground state [14].

Understanding the mechanism underlying the emission of near-threshold harmonics is expected to be a complex task. Several studies have indicated that the generation of NTHs is influenced by various factors, including long and short quantum orbits [18], multirescattering processes [19], and Rydberg states [20]. Unlike above-threshold high-order harmonics, which can be explained by the standard three-step model, NTHs are characterized by the presence of the Coulomb potential from the ion core, significantly altering the trajectories of tunneling electrons. The interpretation of NTH generation in terms of contributions from multiple trajectories and their interference lacks predictive power. Additionally, laboratory observations of NTHs depend on the phase-matching conditions of harmonics in the gas medium, highlighting the need for systematic theoretical simulations of NTHs. Previous experimental findings have also revealed significant differences in the spatial distribution of NTHs, providing valuable insights into the generation mechanisms of NTHs and offering rich information for further investigation [10].

*cjin@njust.edu.cn

To accurately calculate the NTH spectra for individual atoms, the target atom is typically treated as a one-electron system, and the three-dimensional time-dependent Schrödinger equation (3D-TDSE) is solved. Unlike above-threshold harmonics where the quantitative rescattering theory (QRS) model provides a simple approach to calculate harmonics from each atom [21], in NTH, replacing QRS with 3D-TDSE for hundreds of laser intensities in propagation calculations would require significant computational resources. Thus, full macroscopic propagation calculations are rarely performed. Recently, there has been a growing interest in applying artificial intelligence and machine learning techniques to enhance computational methods in physical sciences [22]. The combination of deep learning methods with strong-field physics has shown promising results [23–29]. Deep learning can directly predict final results and reconstruct high-resolution spectra [28], or even predict the time-dependent induced dipole moment of HHG [29]. These methods alleviate the computational limitations of conventional semiclassical approaches and offer new possibilities to tackle problems with high computational costs. More recently, a convolutional neural network has been trained to simulate HHG [30], offering a method that applies the neural network to investigate the generation of HHG.

In this article we propose an approach that utilizes a fully connected neural network as a surrogate model to replace the computationally demanding 3D-TDSE model in macroscopic propagation calculations. Our method allows for a comprehensive and systematic investigation of NTH generation based on the 3D-TDSE, analyzing both microscopic mechanisms and macroscopic propagation, enabling direct comparisons with experimental observations.

II. METHODS

A. 3D-TDSE

The schematic plot of our model is shown in Fig. 1. First, we use the 3D-TDSE model to calculate single-atom induced-dipole moments in the time domain by varying laser peak intensities and carrier-envelope phases (CEPs) for Ar atoms using an 800-nm linearly polarized laser pulse with a FWHM pulse width of three optical cycles (8.1 fs). The envelope of it is trapezoidal with one cycle on and off. We use 500 laser intensities ranging from 0.5×10^{14} W/cm^2 to 3.5×10^{14} W/cm^2 and 100 CEPs ranging from 0 to 2π, resulting in a total of 50 000 data points (500×100) as the input data set for our neural network. The 3D-TDSE describing the dynamics of the electron in the velocity gauge is

$$i\frac{\partial}{\partial t}\psi(\mathbf{r},t) = \left[\frac{1}{2}(\boldsymbol{p} - \mathbf{A}(\mathbf{r},t))^2 + V(\mathbf{r})\right]\psi(\mathbf{r},t), \quad (1)$$

where $\psi(\mathbf{r},t)$ is the electron wave function, $\boldsymbol{p}$ is the momentum operator, and $\mathbf{A}(\mathbf{r},t)$ is the vector potential of the laser field. In the dipole approximation, the vector potential $\mathbf{A}(\mathbf{r},t)$ of is space independent and can be written as

$$\mathbf{A}(\mathbf{r},t) = \mathbf{A}(t) = \int E(t)dt = \int E_0 f(t)\cos(\omega t)dt, \quad (2)$$

where $E(t)$ is the laser electric field, E_0 is the amplitude of the laser electric field, and $f(t)$ is the laser envelop. The

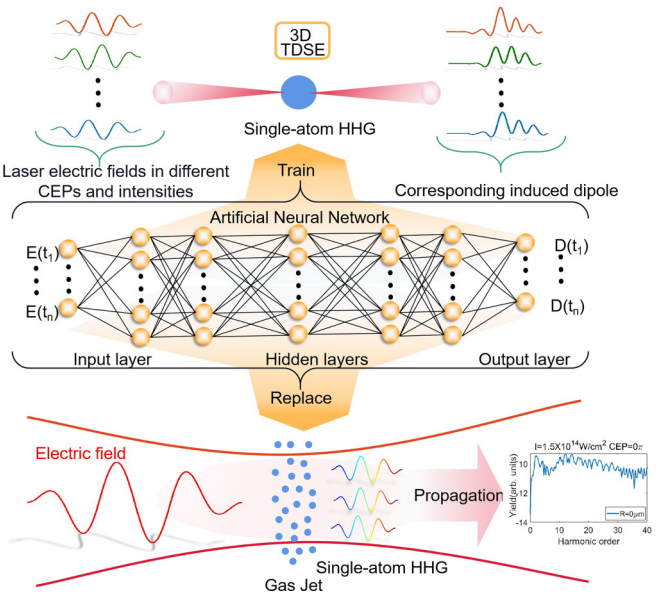

FIG. 1. Schematic plot of the numerical model for computing microscopic and macroscopic NTH.

expression of the laser envelop is

$$f(t) = \begin{cases} t/T & (0 \leqslant t \leqslant T) \\ 1 & (T < t < 2T) \\ (T-t)/T & (2T \leqslant t \leqslant 3T) \end{cases}, \quad (3)$$

where T is the optical cycle of the laser field and t is the time. $V(\mathbf{r})$ is the effective potential, and in our paper, the Tong-Lin potential is used to simulate Ar [31], which is a widely used effective potential and can accurately model excited states and their interaction with electric fields in strong-field scenarios [32]. The 3D-TDSE is solved in the spherical coordinates, in which the wave function $\psi(\mathbf{r},t)$ is expanded by spherical harmonics $|l,m\rangle$,

$$\psi(\mathbf{r},t) = \sum_{l,m}\frac{R_{lm}(\mathbf{r},t)}{r}|l,m\rangle, \quad (4)$$

where $R_{lm}(\mathbf{r},t)$ is the radial part of the wave function. This radial wave function is discretized by a finite-element discrete-variable representation method. The time propagation of the TDSE is calculated by the split-Lanczos method with the time step fixed at $dt = 0.01$ a.u. The initial wave function is prepared by the imaginary-time propagation. The details of the numerical solution to the TDSE can be found in [33]. The induced dipole moment is given by

$$d(t) = \langle\psi(\mathbf{r},t)|\mathbf{r}|\psi(\mathbf{r},t)\rangle. \quad (5)$$

B. Neural network

Second, a fully connected multilayer neural network is utilized for training the input data set. The detailed parameters of the neural network can be found in Table I. The compiler used here is PyTorch, an open-source Pythonmachine learning library. More information about PyTorch can be found on their website [34]. The input data set consists of the laser

TABLE I. Neural network parameters.

Compiler:	PyTorch	Train data:	60%
Epochs:	40 000	Valid data:	20%
Pred data:	20%	Hidden dim:	2048
Hidden layers:	5	Optimizer:	Adam
Lr:	$5 \times 10^{-5} \times$ f(t)[a]	Batch size:	32
L2:	0		

[a]f(t)=0.1 if: epochs = 2.5×10^4, 3.0×10^4, 3.5×10^4.

electric field and the induced dipole moment calculated from the 3D-TDSE. We consider 500 laser intensities ranging from 0.5×10^{14} W/cm^2 to 3.5×10^{14} W/cm^2, as well as 100 CEP values ranging from 0 to 2π. This results in a total of 50 000 data points (500×100) forming the input data set for our neural network. Increasing the amount of input data enhances the stability of the trained results; however, it should not be less than 10 000 to maintain training accuracy and stability. The training data set is randomly divided into three groups in a ratio of 6:2:2, namely, train data, validation data, and prediction data. The neural network architecture consists of one input layer, five hidden layers, and one output layer. Each layer comprises 2048 coefficients, including weight and bias terms. These terms correspond to a time interval of $\Delta t = 0.16$ a.u. in the time domain. In the input layer, the laser electric field in the time domain is divided into 2048 points, denoted as $E(t_i), i = 1 : 2048$. In the hidden layer, each node is connected to the corresponding $E(t_i)$ from the input layer through weights and biases, based on the following formula:

$$a_j = \sum_i W_{i,j} E(t_i) + b_j. \tag{6}$$

Here a_j represents the value of the node, $W_{i,j}$ denotes the weight, and b_j represents the bias in each node. This process is repeated for each subsequent hidden layer, linking nodes in a similar manner until all nodes are transmitted to the output layer. The coefficients in each layer are adjusted through back-propagation algorithms until the mean square error (MSE) between the output-induced dipole and the input dipole is less than 10^{-8}. We have chosen to utilize the Adam algorithm as our optimizer, which is a well-established stochastic optimization method [35].

The MSE of the final training results is influenced by two factors: (1) the input data set and (2) the neural network structure. The input data set should contain at least 10 000 data points to ensure stability and accuracy. Additionally, a stronger correlation between the laser electric field and the induced dipole moment leads to better training outcomes. Thus the target for training is the induced dipole moment in the time domain rather than the spectrum in the frequency domain. To decrease the MSE, various parameters in the neural network need to be appropriately adjusted, such as the number of layers, training epochs, and learning rate. Increasing the number of hidden layers and the number of coefficients in each layer enhances the precision of the neural network output. However, it also increases the computational cost in terms of time and memory usage. The learning rate, denoted as Lr, is a crucial hyperparameter in the network training process. A learning

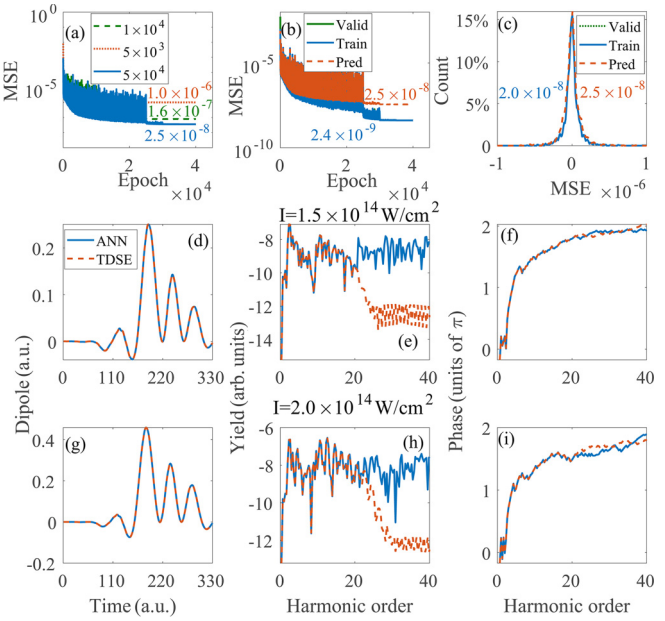

FIG. 2. (a) The MSE of the train data set trained from the different amounts of the input data set. (b) The MSEs between the output-induced dipole and the input-induced dipole as a function of epoch. (c) The distributions of the MSE in different data sets. (d)–(i) The induced dipole moment, the harmonic spectra, and the phase of the harmonics calculated by the artificial neural network (ANN) and the TDSE when the laser intensity is 1.5 $\times 10^{14}$ W/cm^2 and 2.0×10^{14} W/cm^2 and the CEP is 0.

rate that is too high may make it difficult for the network to converge, while one that is too small may cause convergence to local minima. To strike a balance, we set the learning rate to gradually decrease as the number of training epochs increases. The batch size determines the number of parameters passed to the program during each iteration of training. If the batch size is too large, the network may converge to local minimums, and if it is too small, the training results may be erratic. Selecting an appropriate batch size is important for achieving optimal training outcomes.

Figure 2(a) presents the trained MSE using different amounts of 3D-TDSE data. It is observed that when the amount of 3D-TDSE data is 5.0×10^3, the MSE of the train data set is roughly 1.0×10^{-6}, and when it is increased to 5.0×10^4, the MSE decreases to 2.5×10^{-8}. Based on the Fourier transform relationship between the time domain and frequency domain, in order to obtain accurate NTH spectra (in this case, up to the 13th order for 800 nm), the MSE of the induced dipole moment should be less than 1.0×10^{-7}. Therefore, to accurately calculate the harmonic spectrum, it requires a substantial amount of 3D-TDSE data, with a minimum threshold of 1.0×10^4. Figure 2(b) displays the mean square error MSE between the output-induced dipole and the input-induced dipole as a function of the epoch. It was observed that as the training epoch increased, the MSE decreased. At an epoch of 4.0×10^4, the MSEs were 2.5×10^{-8} for the valid data set and the pred data set, while in the train data set it was 2.4×10^{-9}. Figure 2(c) displays the distribution of the MSE among different data sets. The distribution

of the MSE follows a Gaussian distribution, with a FWHM of 2.5×10^{-8} for both the valid data set and pred data set, and 2.0×10^{-8} for the train data set. Figures 2(a), 2(b), and 2(c) demonstrate that the induced dipole moments trained based on the neural network exhibit high precision (2.5×10^{-8}) and good error distribution—both necessary conditions for replacing the 3D-TDSE in the calculation of macroscopic propagation.

In Figs. 2(d)–2(i), we present several examples of the induced dipole moment, harmonic spectrum, and the phase of the harmonics obtained from the trained neural network (blue solid line). It is important to highlight that in the training process, maintaining stability and accuracy of the trained results is crucial. Oscillation of induced dipole moments in the time domain between positive and negative values can introduce instability and lead to significant errors. To overcome this issue, we employ a technique where a constant value is added to each induced dipole moment, ensuring they remain consistently positive during training. Subsequently, when utilizing the neural network to calculate the macroscopic propagation of NTH, the applied constant value is subtracted, guaranteeing result accuracy. In the figures presented, the displayed induced dipole moments reflect the subtracted value, which can be directly employed for calculating the macroscopic propagation of NTH.

By comparing these results with those calculated from the TDSE model (red dash line), we observe that the induced dipole moment in the time domain is nearly identical. However, there are some differences in the high-order harmonic spectra and their phase. These variations occur at the same order (21st) for different laser intensities [see Figs. 2(e), 2(h), and 2(b)], implying that they are independent of the laser intensity. This difference arises from the error in the trained induced dipole moment. The harmonic spectra are generated from the Fourier transform of the induced dipole moment in the frequency domain. Therefore the high-order harmonic spectra correspond to the rapid and small fluctuations of the induced dipole moment in the time domain. As the MSE between the induced dipole moment trained by our model and the dipole moment obtained from 3D-TDSE calculations is approximately 2.5×10^{-8}, the harmonic spectra calculated from the trained dipole moment are accurate for low-order harmonics but show some differences in high-order harmonics. One potential solution to this issue is to increase the number of layers and training epochs in order to decrease the MSE of the neural network. However, in this study we are primarily focused on the accuracy of the near-threshold harmonics, which are adequately represented in the trained harmonic spectra. Besides, we can also find that there is a suppression of the yield of the 7th and 9th harmonics compared with the 11st and 13rd harmonics. These phenomena have been observed experimentally in [36] and attributed to the interaction between the Rydberg state and the laser field. In Fig. 3 we present the induced dipole moment, harmonic spectra, and phase of the harmonics for different CEPs at an intensity of $2.5 \times 10^{14}\,\mathrm{W/cm^2}$. Despite significant changes in the induced dipole moment, our trained model accurately reproduces the dipole moment, harmonic spectra, and phase of the harmonics.

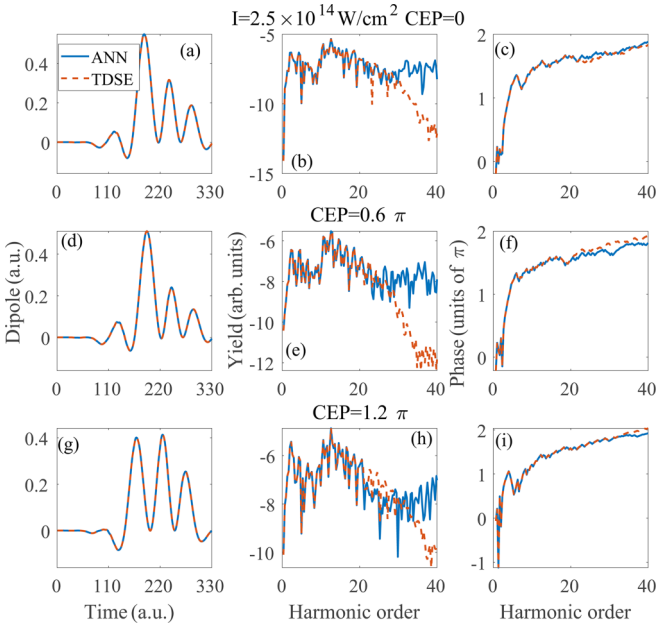

FIG. 3. (a)–(i) The induced dipole moment, the harmonic spectra, and the phase of the harmonics calculated by the ANN and the TDSE when the laser intensity is $2.5 \times 10^{14}\,\mathrm{W/cm^2}$ and the CEP is 0, 0.6π, and 1.2π.

Moreover, in Fig. 4 we have presented some poor results obtained from the trained neural network that corresponded to an MSE larger than 1.0×10^{-7}. It can be observed that the poor results mainly occurred under low laser intensity ($<1.0 \times 10^{14}\,\mathrm{W/cm^2}$) and situations where the induced

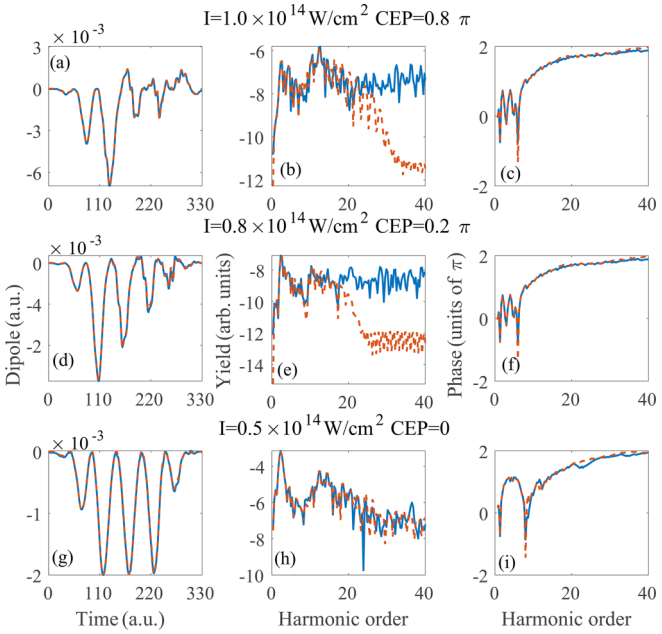

FIG. 4. (a)–(c) The induced dipole moment, the harmonic spectra, and the phase of the harmonics calculated by the ANN and the TDSE when the laser intensity is $1.0 \times 10^{14}\,\mathrm{W/cm^2}$ and the CEP is 0.8π. (d)–(f) The same as (a)–(c), but the laser intensity is $0.8 \times 10^{14}\,\mathrm{W/cm^2}$ and the CEP is 0.2π. (g)–(i) The same as (a)–(c), but the laser intensity is $0.5 \times 10^{14}\,\mathrm{W/cm^2}$ and the CEP is 0.

dipole underwent drastic changes in the time domain. The reason for this is that, on the one hand, the low induced dipole moment occupied a small proportion of the total MSE compared to high laser intensity. On the other hand, the drastic changes in the induced dipole moment were more difficult to replicate in the neural network. From Fig. 4 we notice that this error mostly affects the yield of harmonics and the induced dipole moment, while the phase of harmonics is less affected. In addition, we also need to emphasize that the trained neural network is only valid in the range of the input data set, i.e., from $0.5 \times 10^{14}\,\mathrm{W/cm^2}$ to $3.5 \times 10^{14}\,\mathrm{W/cm^2}$ for laser intensities and from 0 to 2π for CEPs. Expanding the calculation range will lead to the instability of the calculation results.

C. Macroscopic propagation

Finally, the trained neural network is implemented as a surrogate model to compute the single-atom induced dipoles in the macroscopic propagation of NTH. The propagation theory that gives a macroscopic response of NTH to the medium is obtained from our previous paper [37]. The propagation of NTH in the medium is described by the equation

$$\nabla^2 E_h(r,z,t) - \frac{1}{c^2}\frac{\partial^2 E_h(r,z,t)}{\partial t^2} = \mu_0 \frac{\partial^2 P_{nl}(r,z,t)}{\partial t^2}, \tag{7}$$

where

$$P_{nl}(r,z,t) = [n_0 - n_e(r,z,t)]x(r,z,t), \tag{8}$$

$$n_e(t) = n_0\left\{1 - \exp\left[-\int_{-\infty}^{t}\omega(\tau)d\tau\right]\right\}. \tag{9}$$

$P_{nl}(r,z,t)$ is nonlinear polarization generated by the medium, n_0 is the neutral atom density, $n_e(t)$ is free-electron density, and $\omega(\tau)$ is tunnel ionization rate which can be calculated from the Ammosov-Delone-Krainov (ADK) theory [38]. The $x(r,z,t)$ is the induced dipole moment calculated from the neural network. We assume that in low gas pressure, there is no ionization effect of the medium on the fundamental laser field and the effects of absorption and free-electron dispersion are negligible. Only the phase gradient of the fundamental Gaussian beam and the phase of the induced dipole moment will affect the macroscopic propagation process. The temporal derivative in the above equation can be eliminated by Fourier transform:

$$\nabla_\perp^2 E_h(r,z',\omega) - \frac{2i\omega}{c}\frac{\partial E_h(r,z',\omega)}{\partial z'} = -\mu_0\omega^2 P_{nl}(r,z',\omega), \tag{10}$$

where

$$E_h(r,z',\omega) = \hat{F}[E_h(r,z,t)], \tag{11}$$

$$P_{nl}(r,z',\omega) = \hat{F}[P_{nl}(r,z,t)]. \tag{12}$$

Here $\hat{F}$ is the Fourier transform operator acting on the temporal coordinate. It is worth noting that we have compared our calculation result based on this model with the experiment measurement, and the results show that our model can accurately calculate NTH, showing consistency with the experimental measurements presented in [12].

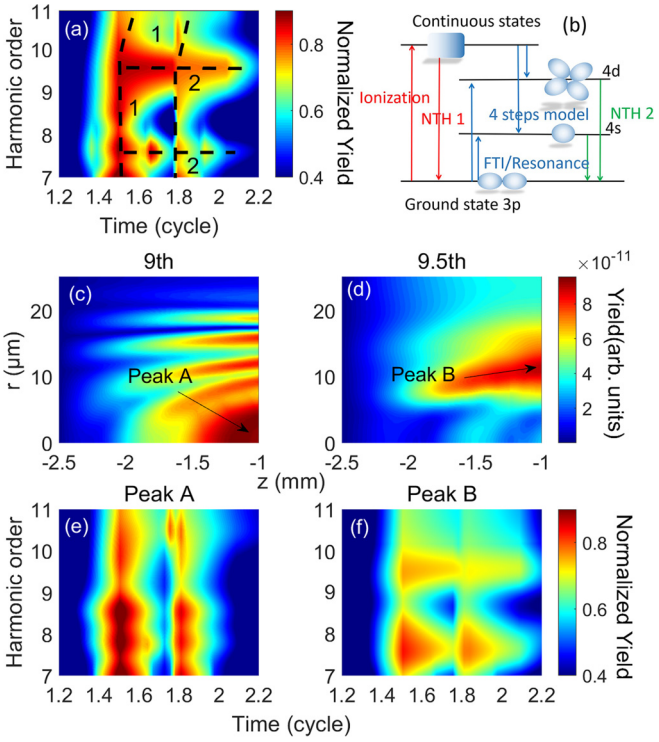

FIG. 5. (a) Time-frequency analysis of the NTH in one optical cycle. (b) Diagrammatic sketch of the generation of NTH 1 and 2. (c), (d) Evolution of the harmonic yields in space (inside gas medium) for H9 and H9.5, respectively. The color boxes of (c) and (d) are the same and uniformly displayed in (d). (e), (f) Time-frequency analysis for the NTH at peak A and peak B, respectively. The color boxes of (e) and (f) are normalized and identical, and are displayed uniformly in (f).

III. RESULTS AND DISCUSSION

We first examine the microscopic features of NTH emissions at the single-atom level using a laser intensity of $2.0 \times 10^{14}\,\mathrm{W/cm^2}$ and a CEP of 0. Time-frequency analysis for NTHs around the 9th harmonic (H9) in one optical cycle is displayed in Fig. 5(a), using the synchrosqueezing transform to clearly see emission structures in the low-frequency regions [19]. Our analysis reveals two types of NTH radiation: NTH 1, which is continuous in the energy domain with an obvious chirp characteristic and has a generation mechanism similar to that of HHG emission caused by long electron trajectories [10,19]; and NTH 2, which has a narrow energy range around 0.4271 a.u. (H7.5) and 0.5410 a.u. (H9.5) and a long duration (> 0.25 optical cycles). These two NTHs have been observed and studied in prior research [12,14,18,20]. The generation mechanism of NTH 1 and NTH 2 is depicted in Fig. 5(b). NTH 1 is considered to originate from the ionization of electrons from the ground state to the continuum state. Upon the reversal of the laser field and subsequent suppression of the core potential, some electrons can undergo a harmoniclike transition from the continuum state back to the ground state, resulting in the generation of NTH 1 [18]. On the other hand, the generation of NTH 2 involves the excitation of electrons from the ground state to either the Rydberg states of $4s$ with an energy of 0.4271 a.u. or $4d$ with an energy of

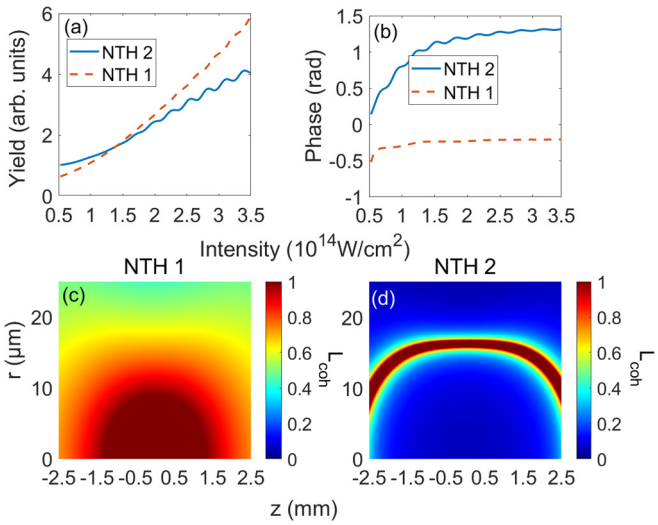

FIG. 6. Dependence of (a) the yields and (b) the phase of the NTH 1 and NTH 2 on laser intensity. (c), (d) Coherence length of NTH 1 and NTH 2 as a function of the propagation distance (z) and the radial distance (r). The color boxes of (c) and (d) are normalized and identical, and are displayed uniformly in (d).

0.5410 a.u. This process can occur through frustrated tunneling ionization (FTI) [14], resonance excitation [12], or the four-steps model [20]. Subsequently, the electrons transition from these Rydberg states to the ground state $3p$, leading to the production of NTH 2. In our paper we refer to the pathway of NTH 1 as a harmoniclike transition and the pathway of NTH 2 as a resonant transition.

Next, we examine the macroscopic properties of NTH. Figures 5(c) and 5(d) show the evolution of harmonic yields in space for H9 and H9.5, respectively, as calculated with the macroscopic propagation model based on the neural network. The driving Gaussian beam has a beam waist of 25 μm at focus, and a 1.5-mm-long gas medium with uniform distribution is located 1.0 mm before laser focus. In Fig. 5(c), H9 exhibits a multipeaked structure, with the first peak occurring on axis at $r = 0$ μm (peak A), the second peak appearing at $r = 12$ μm, and the third peak located at $r = 15$ μm. On the other hand, H9.5 only has one peak at around $r = 12$ μm (peak B) in Fig. 5(d). Figures 5(e) and 5(f) depict the time-frequency analysis for peaks A and B, respectively. It is observed that peak A is solely from the contribution of NTH 1, while peak B only includes the contribution of NTH 2. In other words, the emissions of NTH 1 and NTH 2 can be spatially separated in the exit plane of the gas medium, with NTH 1 primarily focusing on the axis and NTH 2 being concentrated of axis. Note that such separation can only be achieved after the harmonics propagate a certain distance in the medium.

Finally, we discuss the phase-matching conditions that give rise to the different spatial distributions of the two types of NTH. In Fig. 6(a) we calculate the dependence of the yields of NTH 1 and NTH 2 on laser intensity. At low intensities ($<1.5 \times 10^{14}$ W/cm^2), NTH 2 is stronger than NTH 1, while the opposite is true at high intensities. This competitive relationship between NTH 1 and 2 was also observed in experiments [12]. Moreover, we fit the intensity dependence of the NTH 1 and 2 based on the fitting function and coefficients:

$$I_1 = a_1 e^{b_1 I} + c_1, \tag{13}$$

$$I_2 = a_2 e^{b_2 I} + c_2 \quad (I < 1.5 \times 10^{14}\ \text{W/cm}^2),$$
$$I_2 = a_2 e^{b_2 I} + c_2 + a_3 \sin(dI) \quad (I > 1.5 \times 10^{14}\ \text{W/cm}^2), \tag{14}$$

where $a_1 = 0.004\,042$, $b_1 = 0.2576$, $c_1 = -0.003\,474$, $a_2 = 0.031\,56$, $b_2 = 0.2231$, $c_2 = -0.002\,071$, $a_3 = 0.000\,423\,5$, and $d = 20.51$. We can find that the yield of NTH 1 grows as a function of exponential function with the increase of laser intensity. For NTH 2, the yield grows exponentially when the laser intensity is below 1.5×10^{14} W/cm^2 but exhibits oscillatory behavior when the laser intensity is higher. This yield dependence has been observed in the NTH of Xe in experiments [10] and strong-field ionization of hydrogen [39,40], where it is associated with channel closing. In the NTH generation, as discussed above, two mechanisms are involved: harmoniclike transition and resonant transition. The weight of each transition depends on the ionization process and the motion of the electron in the laser field, which are influenced by the laser parameters and the potential of the target. When the total number of the electrons is fixed, harmoniclike and resonant transitions compete with each other. Under low-laser-intensity conditions, ionization becomes more challenging, leading to a relatively weaker harmoniclike transition. As a result, the resonant transition predominates. Conversely, with the laser intensity increasing, the harmoniclike transition increases. At high laser intensity, the harmoniclike transition dominates and limits the resonant transition, resulting in the oscillating increase of resonant transition. Figure 6(b) illustrates the dependence of the phase of NTH 1 and NTH 2 on laser intensity. We also fit them according to the fitting function and coefficients:

$$\varphi_1 = \beta_1 \ln(\alpha_1 I) + \gamma_1, \tag{15}$$

$$\varphi_2 = [\beta_2 \ln(\alpha_2 I) + \gamma_2]\kappa \sin(\omega I), \tag{16}$$

where $\beta_1 = 0.1058$, $\alpha_1 = 0.025\,62$, $\gamma_1 = 0.030\,11$, $\beta_2 = 0.6766$, $\alpha_2 = 1.8125$, $\gamma_2 = 0.2031$, $\kappa = 0.043\,51$, and $\omega = 25.125$. Both are in the form of a logarithmic function, but the phase of NTH 1 approaches a negative constant (–0.2 rad) as laser intensity increases, while the phase of NTH 2 is always a positive number and becomes closer to 1.2 rad as laser intensity increases. Since the Rydberg states of $4s$ and $4d$ are more sensitive to the laser field compared to the continuum states, the phase of NTH 2 changes more rapidly with the laser field.

Based on the dependence of calculated yield and phase of NTHs on laser intensity, we can calculate the phase-matching conditions of NTH 1 and 2. Since the gas pressure in this study is assumed to be low, the electric fields at the center and exit of the gas target do not experience significant changes compared to that at the entrance, and phase mismatch resulting from neutral gas and free-electron dispersion can be neglected. Thus the phase mismatch of NTH can be described as follows:

$$\Delta k = \Delta k_{NTH} + \Delta k_G, \tag{17}$$

where Δk_{NTH} is the phase mismatch caused by the single-atom induced dipole of the two kinds of NTHs, and Δk_G is the phase mismatch due to the phase gradient of the fundamental Gaussian beam. The coherence length is defined as $l_{\text{coh}} = \pi/\Delta k$. Figures 6(c) and 6(d) depict the map of coherence length of the two individual NTHs as a function of propagation distance (z) and radial distance (r). It clearly shows that NTH 1 exhibits optimal phase matching close to the axis, suggesting that it is mainly generated along the axis. On the other hand, the coherence length of NTH 2 is maximum when $r = 10\,\mu$m at $z = -2.5$ mm. When NTH 2 propagates along the z direction, the position with optimal phase matching shifts from $r = 10\,\mu$m to $r = 15\,\mu$m when $z = 0$ mm. Due to the symmetry of the Gaussian beam, the symmetry of NTH 2 is preserved as it propagates from $z = 0$–2.5 mm. Based on these phase-matching conditions, NTH 1 can be selected and enhanced on the axis, while NTH 2 can be strengthened of axis by adjusting the laser parameters.

IV. SUMMARY

In summary, we have demonstrated a method that utilizes artificial neural networks to compute the single-atom induced dipoles from the 3D-TDSE model. This enables us to accurately perform macroscopic propagation for near-threshold harmonics (NTHs) and explain some phenomena observed in experiments. We have revealed that there are two pathways, i.e., harmoniclike and resonant transition, in the microscopic NTH. Due to their different yield and phase dependence on the driving laser intensity, they can be spatially separated after propagating in the gas medium. This work not only provides insights into the generation of macroscopic NTHs but also presents an effective solution to overcome the problem of highly computational costs in NTH generation, as well as in other strong-field physics problems.

Furthermore, our research on the generation mechanisms of NTHs holds significant value for further exploration. However, it is important to note that our discussions are based on the one-electron system 3D-TDSE and may not include certain structural effects [15]. In future studies it would be valuable to explore these effects as a potential research directions. Furthermore, acknowledging that our current discussion of the NTH generation mechanism is qualitative and phenomenological, we propose that future investigations should concentrate on employing novel models that incorporate precise mathematical definitions and physics formulas. This approach will enable a more comprehensive and quantitative analysis of the phenomenon.

ACKNOWLEDGMENTS

We would like to express our gratitude to Prof. C. D. Lin at Kansas State University for the valuable discussions and suggestions. This work was supported by the National Natural Science Foundation of China (NSFC) under Grants No. 12204238, No. 12274230, and No. 11834004, the Natural Science Foundation of Jiangsu Province under Grant No. BK20220925, funding of Nanjing University of Science and Technology (NJUST) under Grant No. TSXK2022D005, and the Fundamental Research Funds for the Central Universities through Grant No. 30923010926.

[1] F. Krausz and M. Ivanov, Rev. Mod. Phys. **81**, 163 (2009).
[2] C. D. Lin, A. T. Le, C. Jin, and H. Wei, *Attosecond and Strong-Field Physics: Principles and Applications* (Cambridge University Press, Cambridge, England, 2018).
[3] P. B. Corkum, Phys. Rev. Lett. **71**, 1994 (1993).
[4] G. Sansone, E. Benedetti, F. Calegari, C. Vozzi, L. Avaldi, R. Flammini, L. Poletto, P. Villoresi, C. Altucci, R. Velotta *et al.*, Science **314**, 443 (2006).
[5] T. Popmintchev, M. C. Chen, D. Popmintchev, P. Arpin, S. Brown, S. Ališauskas, G. Andriukaitis, T. Balčiunas, O. D. Mücke, A. Pugzlys *et al.*, Science **336**, 1287 (2012).
[6] J. Itatani, J. Levesque, D. Zeidler, H. Niikura, H. Pepin, J. C. Kieffer, P. B. Corkum, and D. M. Villeneuve, Nature (London) **432**, 867 (2004).
[7] C. Vozzi, M. Negro, F. Calegari, G. Sansone, M. Nisoli, S. D. Silvestri, and S. Stagira, Nat. Phys. **7**, 822 (2011).
[8] L. He, S. Sun, P. Lan *et al.*, Nat. Commun. **13**, 4595 (2022).
[9] C. Gohle, T. Udem, M. Herrmann, J. Rauschenberger, R. Holzwarth, H. A. Schuessler, F. Krausz, and T. W. Hänsch, Nature (London) **436**, 234 (2005).
[10] D. C. Yost, T. R. Schibli, J. Ye, J. L. Tate, J. Hostetter, M. B. Gaarde, and K. J. Schafer, Nat. Phys. **5**, 815 (2009).
[11] A. Cingöz, D. C. Yost, T. K. Allison, A. Ruehl, M. E. Fermann, I. Hartl, and J. Ye, Nature (London) **482**, 68 (2012).
[12] M. Chini, X. Wang, Y. Cheng, H. Wang, Y. Wu *et al.*, Nat. Photon. **8**, 437 (2014).
[13] A. Ferré *et al.*, Nat. Photon. **9**, 93 (2015).
[14] H. Yun, J. H. Mun, S. I. Hwang *et al.*, Nat. Photon. **12**, 620 (2018).
[15] M. F. Zhu, J. Zhang, L. Q. Hua, Z. R. Xiao, S. P. Xu, X. Y. Lai, and X. J. Liu, Phys. Rev. A **104**, 043111 (2021).
[16] B. C. Wang, Y. F. Zhang, P. F. Lan, C. Y. Zhai, M. Li, X. S. Zhu, J. Chen, P. X. Lu, and C. D. Lin, Phys. Rev. A **103**, 053119 (2021).
[17] S. Beaulieu, S. Camp, D. Descamps, A. Comby, V. Wanie, S. Petit, F. Légaré, K. J. Schafer, M. B. Gaarde, F. Catoire, and Y. Mairesse, Phys. Rev. Lett. **117**, 203001 (2016).
[18] E. P. Power, A. M. March, F. Catoire, E. Sistrunk, K. Krushelnick, P. Agostini, and L. F. DiMauro, Nat. Photon. **4**, 352 (2010).
[19] P. Li, Y. Sheu, C. Laughlin, and S. Chu, Nat. Commun. **6**, 7178 (2015).
[20] W. H. Xiong, J. W. Geng, J. Y. Tang, L. Y. Peng, and Q. Gong, Phys. Rev. Lett. **112**, 233001 (2014).
[21] A.-T. Le, R. R. Lucchese, S. Tonzani, T. Morishita, and C. D. Lin, Phys. Rev. A **80**, 013401 (2009).
[22] K. Mills, K. Ryczko, I. Luchak, A. Domurad, C. Beeler, and I. Tamblyn, Chem. Sci. **10**, 4129 (2019).

[23] N. I. Shvetsov-Shilovski and M. Lein, Phys. Rev. A **105**, L021102 (2022).
[24] A. M. M. Gherman, K. Kovács, M. V. Cristea, and V. Toșa, Appl. Sci. **8**, 2106 (2018).
[25] O. Neufeld, O. Wengrowicz, O. Peleg, A. Rubio, and O. Cohen, Opt. Express **30**, 3729 (2022).
[26] M. Lytova, M. Spanner, and I. Tamblyn, Can. J. Phys. **101**, 132 (2023).
[27] A. Mihailescu, J. Instrum. **11**, C12004 (2016).
[28] X. W. Liu, G. Zhang, J. Li, G. Shi, M. Zhou, B. Huang, Y. Tang, X. Song, and W. Yang, Phys. Rev. Lett. **124**, 113202 (2020).
[29] J. Z. Yan *et al.*, Opt. Express **30**, 35444 (2022).
[30] J. M. Pablos-Marín, P. Marín, J. Serrano, and C. H. García, Comput. Phys. Commun. **291**, 108823 (2023).
[31] X. M. Tong and C. D. Lin, J. Phys. B: At. Mol. Opt. Phys. **38**, 2593 (2005).
[32] H. B. Yao, Q. W. Qu, Z. H. Zhang, J. W. Wang, J. Gao, C. X. Hu, H. Li, J. Wu, and F. He, Phys. Rev. Lett. **130**, 113201 (2023).
[33] J. T. Liang *et al.*, J. Phys. B: At. Mol. Opt. Phys. **53**, 095601 (2020).
[34] https://pytorch.org/.
[35] D. P. Kingma and J. Ba, arXiv:1412.6980.
[36] K. Miyazaki and H. Sakai, J. Phys. B: At. Mol. Opt. Phys. **25**, L83 (1992).
[37] C. Jin, A. T. Le, and C. D. Lin, Phys. Rev. A **79**, 053413 (2009).
[38] M. V. Ammosov, N. B. Delone, and V. P. Krainov, Zh. Eksp. Teor. Fiz. **91**, 2008 (1986) [Sov. Phys. JETP **64**, 1191 (1986)].
[39] Q. G. Li, X.-M. Tong, T. Morishita, C. Jin, H. Wei, and C. D. Lin, J. Phys. B: At. Mol. Opt. Phys. **47**, 204019 (2014).
[40] Q. G. Li, X. M. Tong, T. Morishita, H. Wei, and C. D. Lin, Phys. Rev. A **89**, 023421 (2014).